2019-07-29

Multimodal quantitative imaging of brain cancer in cultured cells

Xin Feng
University of Massachusetts Lowell

Et al.

Research Article | Vol. 10, No. 8 | 1 Aug 2019 | BIOMEDICAL OPTICS EXPRESS 4237
Biomedical Optics EXPRESS

Multimodal quantitative imaging of brain cancer in cultured cells

XIN FENG,[1] ALONA MUZIKANSKY,[2] ALONZO H. ROSS,[3] MICHAEL R. HAMBLIN,[4] PETER R. JERMAIN,[1] AND ANNA N. YAROSLAVSKY[1,4,*]

[1]*Advanced Biophotonics Laboratory, UMASS Lowell, Lowell, MA 01851, USA*
[2]*Massachusetts General Hospital Biostatistics Center, Boston, MA 02114, USA*
[3]*Department of Biochemistry and Molecular Pharmacology, UMASS Medical School, Worcester, MA 01605, USA*
[4]*Wellman Center for Photomedicine, Massachusetts General Hospital, Harvard Medical School, Boston, MA 02114, USA*
**anna_yaroslavsky@uml.edu*

Abstract: Fluorescence emission, polarization and subcellular localization of methylene blue (MB) were studied in four cancerous and two normal human brain cell lines. Fluorescence emission and polarization images were acquired and analyzed. The co-localization of MB with mitochondria, lysosomes and nuclei of the cells was evaluated. Glioblastoma cells exhibited significantly higher MB fluorescence polarization compared to normal astrocytes. Preferential accumulation of MB in mitochondria of glioblastoma cells may explain higher fluorescence polarization values in cancer cells as compared to normal. These findings may lead to the development of a quantitative method for the detection of brain cancer in single cells.

1. Introduction

More than 23,000 new cases of malignant brain tumors are expected to be diagnosed in 2019 in the United States; approximately 18,000 individuals will die from the disease [1]. Gliomas account for approximately 80% of the malignant primary brain tumors, including high-grade, fast-growing glioblastomas. Glioblastoma multiform (GBM) is the most common and lethal intracranial neoplasm in adults [2].

In the majority of cases, brain cancers are diagnosed using histopathology, which relies on the qualitative morphological assessment of tissues and cells, i.e., visual recognition of differences in appearance of cancerous and normal structures. Histopathologic analysis is subjective by nature, being strongly dependent on the training and experience of the pathologist involved. In addition, this method is time-consuming and expensive, as it requires the use of multiple stains and extensive tissue processing. Therefore, the search for objective, quantitative markers of brain cancer, as well as for the methods of cancer detection that could be utilized *in vivo*, remains a hot topic in cancer research [3,4].

Different imaging and spectroscopic approaches to cellular-level characterization of biological specimens are being explored. Recent reports described Raman scattering signals being registered from living cells, with potential applications to cancer diagnosis [5–8] and intraoperative brain tumor delineation [9]. Combined reflectance and fluorescence confocal microscopy using exogenous contrast agents has been used to distinguish gliomas from normal brain tissue [10]. Detection of brain neoplasms using fluorescence signals from protoporphyrin-IX (PpIX) using 5-aminolevulinic acid (ALA) has been proposed [11]. Skala *et al.* and Sun *et al.* demonstrated that NADH fluorescence lifetime imaging (FLIM) could be utilized as a quantitative marker for cancer by measuring the fluorescence lifetime [12,13].

Our group is investigating the potential of fluorescence polarization (FP) imaging [14] for cancer detection. Specifically, we focus on FP exhibited by exogenous methylene blue (MB),

#364428 https://doi.org/10.1364/BOE.10.004237
Journal © 2019 Received 15 Apr 2019; revised 12 Jun 2019; accepted 17 Jun 2019; published 29 Jul 2019

Biomedical Optics EXPRESS

a phenothiazinium dye approved by the United States Food and Drug Administration for several clinical indications [15,16]. Previously, we demonstrated that MB enhanced contrast of brain neoplasms [17,18]. We have also shown that MB FP is significantly elevated in cancerous skin, breast and brain tissues [19–22]. More recently, we developed quantitative imaging techniques permitting FP analysis of single living cells. We showed that cultured human breast cancer cells exhibited significantly higher MB FP as compared to normal breast cells [23]. We also observed higher FP in renal fine-needle aspiration biopsy samples [24].

In this study we investigated MB FP of cultured human brain cells. We tested four glioblastoma cell lines and two normal astrocyte cell lines. Multimodal confocal microscopy was used to provide MB fluorescence emission and quantitative FP images of the cells. In addition, we performed co-localization experiments to evaluate the subcellular accumulation of MB in the brain cells.

2. Materials and methods

2.1 Cell culture and handling

Human glioblastoma cell lines U87-MG, U118-MG, and U251-MG were obtained from the American Type Culture Collection (ATCC, Manassas, VA, USA). The primary glioblastoma cell line, 5075-MG, was provided by Dr. Alonzo Ross (University of Massachusetts Medical School, Worcester, MA). Two normal human astrocyte (NHA) cell lines, Clonetics-NHA and Gibco-NHA, were purchased from Lonza (Walkersville, MD) and Life Technologies (Carlsbad, CA, USA), respectively. 5075-MG and U251-MG cells were maintained as a monolayer culture in Dulbecco's modified Eagle's medium (DMEM, Life Technologies, Carlsbad, CA, USA) supplemented with 10% fetal bovine serum (ATCC, Manassas, VA, USA) and 1% sodium pyruvate (Life Technologies, Carlsbad, CA, USA). U87-MG, U118-MG and Gibco-NHA were cultured as monolayer in DMEM (Life Technologies, Carlsbad, CA, USA) supplemented with 10% fetal bovine serum. Clonetics-NHA was cultured with Astrocyte Growth Medium (AGM) BulletKit (Lonza, Walkersville, MD). All cells were grown at 37°C in 5% CO_2-humidified atmosphere in 75 cm^2 flasks (Life Technologies, Carlsbad, CA, USA). When the cells reached 80% confluency, they were rinsed with phosphate-buffered saline (PBS) (Life Technologies, Carlsbad, CA, USA) and harvested with 0.25% trypsin- ethylenediaminetetraacetic acid (EDTA) (Life Technologies, Carlsbad, CA, USA) solution. After centrifuging, the cells were plated in glass-bottom 4-well 35 mm Petri dishes (In Vitro Scientific, Mountain View, CA, USA) at a density of 10^5 cells per well. The cells were allowed to attach for 24 hours before imaging. All cell lines underwent a maximum of ten passages.

All of the cells were cultured at Wellman Center for Photomedicine, except for the primary glioblastoma cell line, 5075-MG, which was cultured at the University of Massachusetts Medical School.

The cells were transported to the Advanced Biophotonics Laboratory at UMASS Lowell for imaging and analysis. During transportation, cells were kept at 37°C in Leibovitz's L-15 medium (ATCC, Manassas, VA, USA). Prior to staining and imaging, cells were allowed to rest in the incubator (AR36L, Percival Scientific, Perry, IA, USA) for 40 min at a temperature of 37°C and relative humidity (RH) of 95% for recovery. Then the cells were stained with 0.05 mg/ml aqueous solution of MB (0.3 ml per well) for 20 minutes. After staining, the cells were rinsed three times with PBS (Life Technologies, Carlsbad, CA, USA) to reduce background fluorescence. Confocal images of the cells were acquired at the ambient temperature of 18°C. The imaging time of each plate was limited to 30 min, and all plates were imaged within 6 hours after delivery. During the wait time, the cells were kept in the incubator in L-15 medium at a temperature of 37° C and RH of 95%.

Biomedical Optics EXPRESS

2.2 Multimodal confocal imaging

The point scanning multimodal confocal imaging system is illustrated in Fig. 1. A linearly polarized collimated beam emitted by a 642 nm diode laser (Micro Laser Systems, Garden Grove, CA) was used for illumination. The laser beam was scanned across x and y directions using a polygon mirror (Lincoln Laser, Phoenix, AZ) and a galvanometric mirror (General Scanning Inc., Billerica, MA), respectively. The scanning rate was set to 7 frames per second. The laser beam was focused onto the imaging plane by a 63X/1.4NA oil immersion objective (Carl Zeiss, Oberkochen, Germany) which provided a field of view of 205 μm^2. Fluorescence signal emitted from the sample was reflected by a 12-degree dichroic mirror (Iridian Spectral Technologies, Ottawa, Ontario, Canada) with a reflection band between 670 – 740 nm and focused onto a 200 µm diameter pinhole. A 690 nm bandpass filter with full width at half maximum of 40 nm (Chroma Technology Corp., Bellows Falls, VT) was used before the pinhole to further reject the excitation light. Co- and cross-polarized components of the fluorescence emission were separated by a polarizing beam splitter (Karl Lambrecht Co., Chicago, IL) and simultaneously registered by two photomultiplier tubes (PMT) (Hamamatsu, Japan). Elastically scattered light was transmitted though the dichroic mirror, deflected by a non-polarizing beam splitter (Tower Optical, Boynton Beach, FL) and focused onto the 200 µm diameter pinhole of the reflectance PMT. Signal was recorded as 8-bit gray-scale intensity images. The system yielded lateral resolution better than 0.9 µm and axial resolution of 2 µm.

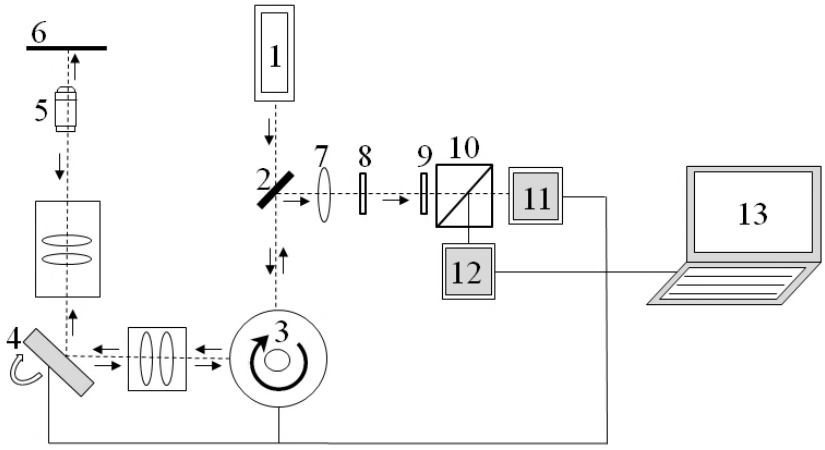

Fig. 1. Schematic of the point scanning confocal fluorescence polarization imaging system. 1 – 642 nm laser, 2 – dichroic mirror, 3 – polygon mirror, 4 – galvanometric mirror, 5 – objective, 6 – sample plane, 7 – focusing lens, 8 – fluorescence filter, 9 – pinhole, 10 – polarizing beam splitter, 11 – PMT for cross-polarized fluorescence, 12 – PMT for co-polarized fluorescence, 13 – computer.

2.3 System calibration

The G factor, which characterizes the sensitivity of the detection channels to polarization, was measured with MB solution (Akorn, Inc., Lake Forest, IL) in phosphate buffered saline (PBS) and glycerol. The system's G factor was determined to be $G = 0.75$, following the formula for co-linear geometry derived by Seigel *et al.* [25]:

$$G = \sqrt{\frac{F_{vv}}{F_{hh}} \times \frac{F_{hv}}{F_{vh}}} \quad (1)$$

where F_{vv} corresponds to the fluorescence emission with vertically polarized excitation and vertically polarized emission, F_{hv} - horizontally polarized excitation and vertically polarized

Biomedical Optics EXPRESS

emission, F_{vh} - vertically polarized excitation and horizontally polarized emission, and F_{hh} - horizontally polarized excitation and horizontally polarized emission.

To validate the *G* factor, fluorescence polarization of each solution was calculated and confirmed with a commercial spectrofluorometer (FluoroMax-4, Horiba, Edison, NJ).

2.4 Data processing

Fluorescence polarization analysis was performed using MetaMorph software (Molecular Devices, Sunnyvale, CA). Co- and cross-polarized fluorescence emission images were thresholded to remove the background and saturated pixels. The low threshold value was selected to be 2, and the high threshold value was selected to be 254. For each cell area, fluorescence emission values were determined from co-polarized $(F_{//})$ and cross-polarized $(F_{\perp})$ fluorescence images. Fluorescence polarization (*FP*) of each cell was calculated using Eq. (2):

$$FP = \frac{F_{//} - G \times F_{\perp}}{F_{//} + G \times F_{\perp}} \tag{2}$$

where *G* is the calibration coefficient determined using formula (1). The fluorescence polarization value of each cell was obtained by averaging over 5 measurements. Data was averaged over each plate, and then averaged over all the plates to get average fluorescence polarization of each cell line.

Fluorescence polarization images were generated in ImageJ (http://rsb.info.nih.gov/ij) using co-polarized $(F_{//})$ and cross-polarized $(F_{\perp})$ fluorescence images. Before image calculation, background was corrected, and images were converted to 32-bit [26]. Fluorescence sum $(F_{//} + G \times F_{\perp})$ and difference $(F_{//} - G \times F_{\perp})$ images were generated using Image Calculator. The fluorescence polarization $(FP = \frac{F_{//} - G \times F_{\perp}}{F_{//} + G \times F_{\perp}})$ image was then calculated using Ratio Plus. NucMed plugin was used to assign pseudo colors to the fluorescence polarization image. Color range was set from 0.10 to 0.34.

2.5 Cell viability assay

After imaging, the cells were stained with 0.4% trypan blue (Sigma-Aldrich, St. Louis, MO) and counted under a light microscope (PrimoVert, Carl Zeiss Microscopy, Peabody, MA) to confirm cell viability. MB stained cells appeared light blue under the microscope, whereas cells stained with both MB and trypan blue appeared purple and were considered dead. Plates with viability > 95% were selected for analysis.

2.6 Co-localization experiments

Previously published manuscripts [27–33] have reported that MB preferentially accumulates in several different intracellular organelles, including mitochondria, lysosomes, and nuclei. To quantitatively investigate the degree of MB co-localization with the nucleus, mitochondria, and lysosomes in the cell lines, we conducted the following experiments. LysoTracker Yellow HCK-123 (Life Technologies) was diluted with growth medium to a final concentration of 100 nM. MitoTracker Green FM (Life Technologies) was dissolved as 1mM stock in DMSO and diluted with growth medium to a final concentration of 50 nM. Incubation time with LysoTracker and MitoTracker was 30 min. Cells were first stained with organelle trackers, and then stained with 0.05 mg/ml MB for 20 min under the same conditions as for the fluorescence polarization imaging experiments. After incubation with the trackers and MB, the cells were labeled for 5 minutes with a nuclei stain, 2 µg/ml Hoechst-33342 (Life Technologies). Fluorescence emission images of live cells were recorded through

Biomedical Optics EXPRESS

a confocal microscope (IX81, Olympus, Tokyo, Japan) with 40X water immersion objective lens. Images were acquired using Olympus FV10-ASW software (Olympus, Tokyo, Japan). During imaging, cells were kept in L-15 medium at 37°C. The degree of MB co-localization with different organelles was evaluated using the Coloc 2 plugin in Image J software. Regions of interest (ROIs) were manually selected to outline the organelles. Subcellular co-localization of MB to nuclei, mitochondria and lysosomes was quantified using Pearson's R values, which were generated for all the imaged cells. For each cell line, the data were averaged over all the imaged cells.

2.7 Statistical analysis

To quantify the significance of differences in fluorescence polarization values obtained in the fluorescence polarization imaging experiments, and Pearson's R values obtained in MB localization experiments, the data were statistically evaluated using a mixed effects linear model [34]. Estimates of the means and standard errors were obtained for each cell line. The significance of the differences between the cancer and normal cell lines was assessed. $P < 0.001$ was considered significant.

3. Results

In total, we imaged the MB fluorescence emission and polarization in 1839 individual cultured human brain cells, including 1054 for glioblastoma cell lines and 785 for normal astrocyte lines. In particular, in the cancerous cells lines, U87-MG, U118-MG, 5075-MG, and U251-MG we imaged 441, 101, 298, and 214 cells, respectively. From the normal cell lines, we imaged 620 cells from Clonetic-NHA and 165 cells from Gibco-NHA. The results are summarized in Table 1. They demonstrate a pronounced difference in fluorescence polarization values between glioblastoma cells and astrocytes. Overall, the average MB FP in glioblastoma cells was higher than that in astrocytes for all the cancer – normal cell line comparisons. As shown in columns 3 and 4 of Table 1, the glioblastoma cell lines, including U87-MG, U118-MG, U251-MG and primary 5075-MG cells had average FP values of 25.25 ± 0.09 $x10^{-2}$, 24.39 ± 0.15 $x10^{-2}$, 24.92 ± 0.11 $x10^{-2}$ and 24.30 ± 0.09 $x10^{-2}$, respectively. The normal Clonetics-NHA had an average FP value of 21.55 ± 0.08 $x10^{-2}$, which is comparable to the average value of 21.46 ± 0.12 $x10^{-2}$ exhibited by Gibco-NHA. The minimal differences in FP values of 13% were obtained for 3 cancer/normal cell line pairs, including U118MG/Clonetic NHA, 5075MG/Clonetic NHA and 5075MG/Gibco NHA. The maximal differences in FP values of 18% were obtained for U87MG/Gibco NHA. Even though these differences are not large on an absolute scale, the small standard errors, shown in column 4 of Table 1, ensure excellent separation between glioblastoma cells and normal astrocytes. Statistical analysis confirmed that the differences between astrocytes and glioblastoma cells were significant for all cell lines pairs ($p<0.0001$).

3.1 Fluorescence emission and polarization of MB

Representative fluorescence emission and polarization (FP) images of two normal human astrocyte and four human glioblastoma cell lines (U87-MG, U118-MG, 5075-MG, and U251-MG) are presented in Figs. 2 and 3, respectively. Figures 2(a)-(f) show fluorescence emission images of cells after 20 min incubation with MB. In all cell lines, the MB fluorescence signal was observed to arise from the entire cell area. However, the fluorescence emission was not distributed evenly across the cell area. In particular, nuclei of the cells exhibited stronger fluorescence. This observation is consistent with known nuclear staining properties of MB [35].

Biomedical Optics EXPRESS

Table 1. Cell line information and percentage differences of MB FP between glioblastoma cells and normal astrocytes (all the cells).

Cell Line	# of Cells	Whole Cell FP		%diff in FP		P Value	
		Average	Standard Error	vs. Gibco-NHA	vs. Clonetic-NHA	vs. Gibco-NHA	vs. Clonetic-NHA
U87-MG	441	25.25 × 10-2	0.09 × 10-2	18	17	<0.0001	<0.0001
U118-MG	101	24.39 × 10-2	0.15 × 10-2	14	13	<0.0001	<0.0001
5075-MG	298	24.30 × 10-2	0.09 × 10-2	13	13	<0.0001	<0.0001
U251-MG	214	24.92 × 10-2	0.11 × 10-2	16	16	<0.0001	<0.0001
Clonetic-NHA	620	21.55 × 10-2	0.08 × 10-2				
Gibco-NHA	165	21.46 × 10-2	0.12 × 10-2				

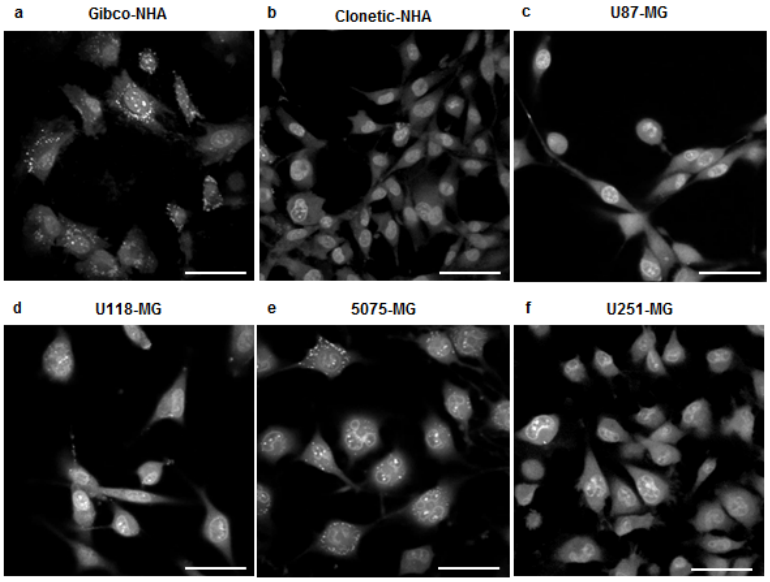

Fig. 2. Methylene blue (MB) fluorescence emission images of normal astrocytes (a, b) and glioblastoma cells (c-f). Cells were stained with 0.05 mg/ml MB. Bar: 50 µm.

The nucleoli and nuclear envelope can be identified clearly in all the cells. Many glioblastoma cells (Figs. 2(c)-(f)), especially primary 5075-MG cells (Fig. 2(e)), display high mitotic activity. Outside the nuclei, a strong signal was observed from the mitochondria and lysosomes of the cells. Corresponding quantitative FP images are presented in Figs. 3(a)-(f). The scale bar color range corresponds to the fluorescence polarization values between 0.10 and 0.34. Figure 3(a) and Fig. 3(b) reveal that the FP in the nucleus of astrocytes was higher, as compared to the rest of the cell. On the other hand, the FP of the GBM cells was distributed more homogeneously and remained high over the entire cell volume (Figs. 3(c)-(f)).

Biomedical Optics EXPRESS

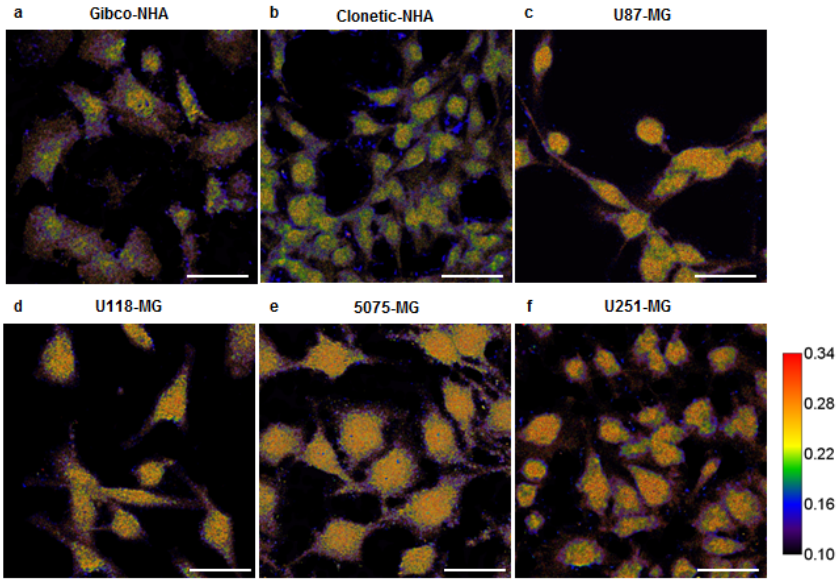

Fig. 3. Methylene blue (MB) fluorescence polarization images of normal astrocytes (a, b) and glioblastoma cells (c-f). Cells were stained with 0.05 mg/ml MB. Bar: 50 µm

The FP images in Fig. 3 demonstrate that the MB FP differences between cancer and normal cells were more pronounced in the region outside of the cell nucleus.

3.2 Subcellular Localization of MB

Results of the co-localization experiments are shown in Fig. 4. For each experiment we imaged and analyzed 31 – 56 cells in each of the different cell lines. The degree of MB co-localization within the cell organelles were quantified by Pearson's *R*-value. As shown in Fig. 4(a), the degree of MB co-localization with the nuclei is uniformly high among all the cell lines. The mean Pearson's *R*-values for U87-MG, U118-MG, 5075-MG and U251-MG were 0.34 ± 0.03, 0.39 ± 0.03, 0.37 ± 0.03 and 0.5 ± 0.03, respectively. For the normal cell lines, the R-values were 0.037 ± 0.02 (Clonetics-NHA) and 0.47 ± 0.03 (Gibco-NHA). No significant differences were observed between astrocytes and glioblastoma cells. MB co-localization with lysosomes is presented in Fig. 4(b). It varied across different cell lines. In particular, U87-MG, U118-MG and Gibco-NHA yielded comparable Pearson's R-values of 0.36 ± 0.03, 0.39 ± 0.03, and 0.34 ± 0.03, respectively. Weaker degrees of co-localization were observed in 5075-MG, U251-MG, and Clonetics-NHA. Their respective R-values were 0.2 ± 0.02, 0.17 ± 0.03, and 0.1 ± 0.03 respectively. Figure 4(c) demonstrates the results of MB co-localization with mitochondria. R-values of glioblastoma cell lines, U87-MG, U118-MG, 5075-MG, and U251-MG were, 0.70 ± 0.05, 0.42 ± 0.04, 0.29 ± 0.04, and 0.36 ± 0.04, respectively. It can be appreciated that the cell line with highest FP, U87-MG, demonstrates the highest degree of MB co-localization with the mitochondrial-tracker, whereas the glioblastoma which presented the lowest fluorescence polarization value, cell line 5075-MG, also yielded the lowest degree of MB co-localization with the mitochondrial tracker. This correlation suggests that the intracellular binding sites of MB play an important role in determining the average FP values within the cells. Both normal cell lines, Clonetic NHA and Gibco-NHA showed a low degree of MB co-localization with mitochondria and yielded Pearson's R-values of 0.17 ± 0.04 and 0.11 ± 0.04, respectively. Thus MB has significantly higher ($p < 0.0001$) degrees of co-localization with mitochondria in glioblastoma cell lines, as compared to those in normal astrocytes in all the normal / cancer cell line comparisons. The affinity of MB to the mitochondria of glioblastoma cells can explain the higher FP observed from cancer cells.

Biomedical Optics EXPRESS

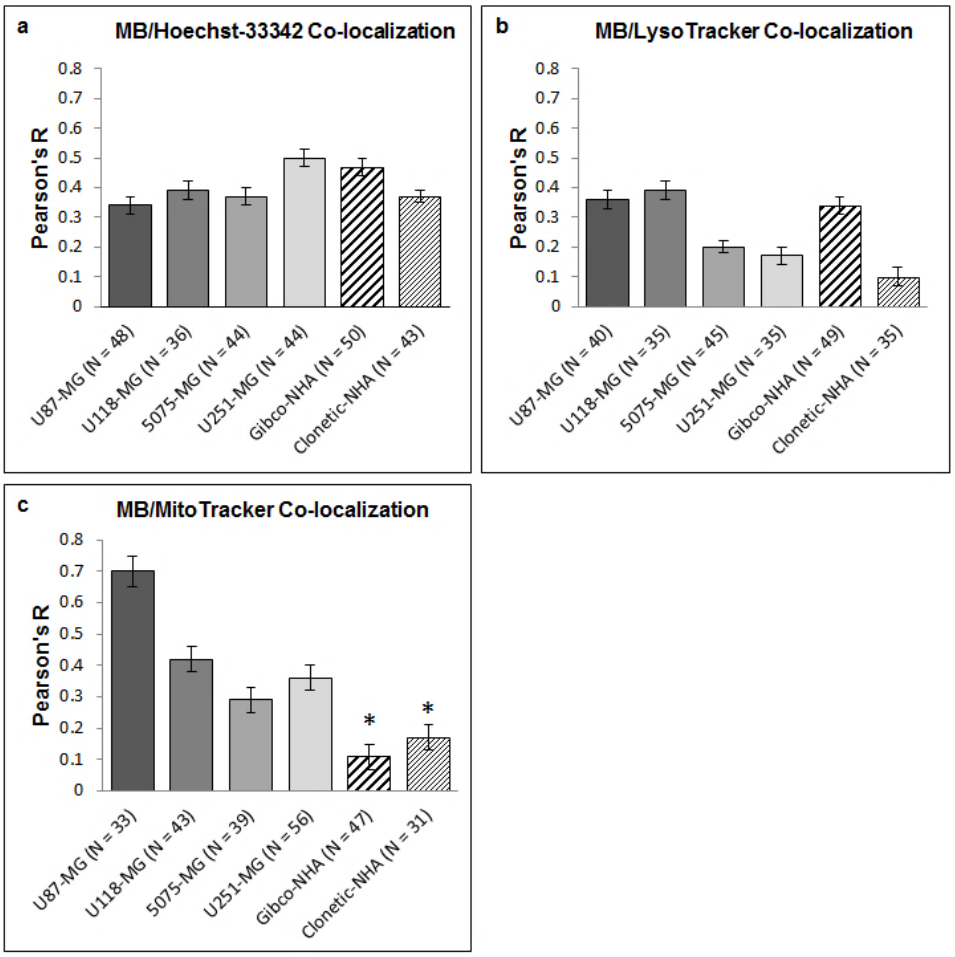

Fig. 4. Degree of co-localization between MB staining and the stain used to visualize (a) nucleus (Hoechst-33342), (b) lysosomes (LysoTracker) and (c) mitochondria (MitoTracker). N is the number of cells analyzed. *p<0.0001

4. Discussion

This study was performed to evaluate multimodal optical imaging for potential use in the detection of brain cancer at the cellular level. Previously, we showed that dye-enhanced confocal reflectance and fluorescence emission imaging could provide morphological details of normal and cancerous brain tissue, comparable to that of H&E histopathology [17,18]. In accordance with our results obtained for brain tissues, fluorescence emission imaging of single cells yielded morphological features similar to those of histopathology. The results of MB fluorescence polarization imaging reveal that cancerous brain cells exhibited significantly higher MB FP as compared to normal astrocytes ($p<0.0001$). We observed that the FP from cancer cells was homogeneously distributed over the entire cell volume, whereas the FP of the normal cells was higher in the nucleus. To validate this observation, we used fluorescence emission images to select cells with clearly outlined nuclei and performed subcellular FP analysis. In particular, we segmented the nuclei of the cells and determined the average MB FP values of the cells with nuclei excluded from the analysis. Then we determined fluorescence polarization of the cell nuclei of these cells. Subcellular FP analysis of 630 cells was conducted. This included 391 cancer cells (U87-MG: 105, U118-MG: 80, 5075-MG:

Biomedical Optics EXPRESS

101, U251-MG: 105) and 239 normal cells (Clonetic-NHA: 136, Gibco-NHA: 103). The results of this analysis are presented in Table 2a-c.

Table 2. Cell line information, MB FP values and percentage differences of MB FP between glioblastoma cells and normal astrocytes. (a) Analysis of the entire cell; (b) analysis of these cells with nuclei excluded; (c) analysis of the cell nuclei.

a	Cell Line	# of Cells	Whole Cell FP	%diff in FP with Gibco-NHA	%diff in FP with Clonetic-NHA	P Value vs. Clonetic-NHA	P Value vs. Gibco-NHA
	U87-MG	105	25.61 ± 0.15 x10-2	19	18		
	U118-MG	80	24.79 ± 0.17 x10-2	15	14	<0.0001	<0.0001
	5075-MG	101	24.51 ± 0.16 x10-2	14	13		
	U251-MG	105	25.67 ± 0.16 x10-2	20	18		
	Clonetic-NHA	136	21.70 ± 0.15 x10-2				
	Gibco-NHA	103	21.47 ± 0.15 x10-2				

b	Cell Line	# of Cells	Cell FP (excluded nucleus)	%diff in FP with Gibco-NHA	%diff in FP with Clonetic-NHA	P Value vs. CloneticNHA	P Value vs. Gibco-NHA
	U87-MG	105	25.13 ± 0.13 x10-2	23	19		
	U118-MG	80	24.15 ± 0.15 x10-2	19	15	<0.0001	<0.0001
	5075-MG	101	23.94 ± 0.14 x10-2	17	13		
	U251-MG	105	25.00 ± 0.15 x10-2	23	18		
	Clonetic-NHA	136	21.05 ± 0.13 x10-2				
	Gibco-NHA	103	20.43 ± 0.14 x10-2				

c	Cell Line	# of Cells	Nucleus FP	%diff in FP with Gibco-NHA	%diff in FP with Clonetic-NHA	P Value vs. CloneticNHA	P Value vs. Gibco-NHA
	U87-MG	105	25.90 ± 0.13 x10-2	14	12		
	U118-MG	80	24.62 ± 0.16 x10-2	8	6	<0.0001	<0.0001
	5075-MG	101	24.45 ± 0.14 x10-2	8	6		
	U251-MG	105	25.76 ± 0.15 x10-2	14	12		
	Clonetic-NHA	136	23.08 ± 0.13 x10-2				
	Gibco-NHA	103	22.73 ± 0.13 x10-2				

As shown in Table 2a, column 3, Gibco-NHA had an average FP value of 21.47 ± 0.15 x10-2, which is comparable to the average value of Clonetics-NHA (21.70 ± 0.15 x10-2). The glioblastoma cell lines, including U87-MG, U118-MG, U251-MG and primary 5075-MG cells had average FP of 25.61 ± 0.15 x10-2, 24.79 ± 0.17 x102, 25.67 ± 0.16 x10-2 and 24.51 ± 0.16 x10-2, respectively. The FP results in Table 2a demonstrate good separation between glioblastoma cells and normal astrocytes. Statistical analysis confirmed that the differences between astrocytes and glioblastoma cells were significant for all cell lines ($p<0.0001$).

As shown in Table 2b, when the nuclei were excluded, Gibco-NHA and Clonetics-NHA had decreased average FP values of 20.43 ± 0.14 x10-2 and 21.05 ± 0.13 x10-2, respectively.

Biomedical Optics EXPRESS

Glioblastoma cell lines, U87-MG, U118-MG, 5075-MG, and U251-MG exhibited average FP of 25.13 ± 0.13 x10-2, 24.15 ± 0.15 x10-2, 23.94 ± 0.14 x10-2, and 25.00 ± 0.15 x10-2, respectively. In comparison to the analysis of the entire cell, larger FP differences between cancer and normal cells were observed when the nuclei were excluded from the analysis. Therefore, excluding the nuclei from the analysis allows for better discrimination of cancer cells from normal cells. In addition, we analyzed the difference in fluorescence polarization exhibited by the nuclei of the normal and cancerous cells. The results are shown in Table 2c. It can be seen that the nuclei of glioblastoma cell lines, U87-MG, U118-MG, 5075-MG, and U251-MG presented average FP values of 25.90 ± 0.13 x10-2, 24.62 ± 0.16 x10-2, 24.45 ± 0.14 x10-2, and 25.76 ± 0.15 x10-2, respectively. The nuclei of the Clonetics-NHA and Gibco-NHA exhibited average FP values of 23.08 ± 0.13 x10-2 and 22.73 ± 0.13 x10-2, respectively. Even though the differences of FP between cancer and normal cells that were observed from the nuclei are smaller in comparison to those obtained from the entire cells, they are still highly significant ($p<0.0001$).

Previous studies have shown that MB displays a high affinity to the mitochondria [27,36], and it is known that mitochondria have increased relative abundance in cancer cells [27]. Our subcellular MB localization experiments confirmed that the degree of co-localization for MB and mitochondria in the cancer cells was significantly higher as compared to normal cells. Mitochondria display several properties consistent with this finding. In particular, the negatively charged inner mitochondrial membrane attracts positively charged, lipophilic molecules such as MB [27]. The degree of dye accumulation is proportional to the mitochondrial membrane potential (MMP) [27], which is increased in various pathologies including brain, breast, renal and pancreatic cancers [37–39]. In addition, the mitochondrial matrix is viscous in comparison with primarily aqueous cytoplasm [40]. Preferential uptake of MB by the mitochondria of the cancer cells, as well as increased viscosity within mitochondria may cause the observed increase in MB FP.

As mentioned above, cancers of the brain, breast, kidney, pancreas, lung and colon are characterized by elevated MMP [37–39]. Therefore, these malignancies may also exhibit increased FP due to binding of MB to the mitochondria. Apart from the current study, our previous work with cultured breast cells [23] and renal FNA specimens [24] support this hypothesis. Overall, the MB FP technique may be capable of accurately diagnosing several types of cancers. However, further studies with clinical brain specimens are required to investigate the utility and sensitivity of MB FP for the detection of brain cancer at early stages.

Our optical imaging technique is rapid, non-destructive and does not necessarily require tissue acquisition and processing. Viability experiments performed in this study revealed that the cells remained viable during and after the experiments. These characteristics point to the possibility of real time, *in vivo* detection of cancers at the cellular level. A wide range of clinical and research applications could utilize this technology to study the early stages of cancer progression in animal models, and also to evaluate new cancer drugs, treatment modalities and protocols. The multimodal imaging approach presents several distinct advantages for analysis of single cells compared to existing methods. The fluorescence images display morphology comparable to histology, while FP images provide a quantitative metric for each cell. The equipment is inexpensive and robust, while the imaging procedure is rapid. Due to the simplicity of data processing and interpretation, quantitative images may be acquired and interpreted by researchers and clinicians without extensive training. Taken together, these features may facilitate wide adoption of the method by cancer researchers, as well as life-science and medical professionals.

5. Conclusions

In summary, our study provided several important results. We demonstrated that human brain cancer cells exhibited significantly higher fluorescence polarization of methylene blue as

Biomedical Optics EXPRESS

compared to normal human brain cells. Greater uptake of methylene blue by mitochondria in cancer cells offers an explanation for the observed increase in fluorescence polarization. Other cancers also exhibit increased mitochondrial membrane potential and therefore may also display increased fluorescence polarization of methylene blue. The results of our study show that the proposed imaging approach may be useful for a broad range of clinical and research applications in brain cancer diagnosis.

Funding

OTC of the University of Massachusetts; US NIH (R01AI050875).

Acknowledgements

We would like to acknowledge Dr. Yulian Ramirez, from UMASS Medical School, Department of Biochemistry and Molecular Pharmacology, and Dr. Yingying Huang, from Wellman Center for Photomedicine, for their assistance with cell culture, as well as Dr. Jenny Zhao from Wellman Center for Photomedicine for help with the co-localization experiments.

Disclosures

The authors declare that there are no conflicts of interest related to this article.

References

1. National Cancer Institute, "Cancer statistics: brain and other nervous system cancer," (2019). https://seer.cancer.gov/statfacts/html/brain.html
2. American Cancer Society, "Types of brain tumors and spinal cord tumors in adults," (2019). http://www.cancer.org/cancer/brain-spinal-cord-tumors-adults/about/types-of-brain-tumors.html
3. W. Szopa, T. A. Burley, G. Kramer-Marek, and W. Kaspera, "Diagnostic and therapeutic biomarkers in glioblastoma: current status and future perspectives," BioMed Res. Int. **2017**(1), 8013575 (2017).
4. F. S. Saadeh, R. Mahfouz, and H. I. Assi, "EGFR as a clinical marker in glioblastomas and other gliomas," Int. J. Biol. Markers **33**(1), 22–32 (2018).
5. A. C. De Luca, K. Dholakia, and M. Mazilu, "Modulated Raman spectroscopy for enhanced cancer diagnosis at the cellular level," Sensors (Basel) **15**(6), 13680–13704 (2015).
6. D. Cialla-May, X. S. Zheng, K. Weber, and J. Popp, "Recent progress in surface-enhanced Raman spectroscopy for biological and biomedical applications: from cells to clinics," Chem. Soc. Rev. **46**(13), 3945–3961 (2017).
7. Y. Zhou, C. H. Liu, Y. Sun, Y. Pu, S. Boydston-White, Y. Liu, and R. R. Alfano, "Human brain cancer studied by resonance Raman spectroscopy," J. Biomed. Opt. **17**(11), 116021 (2012).
8. M. Haifler, I. Pence, Y. Sun, A. Kutikov, R. G. Uzzo, A. Mahadevan-Jansen, and C. A. Patil, "Discrimination of malignant and normal kidney tissue with short wave infrared dispersive Raman spectroscopy," J. Biophotonics **11**(6), e201700188 (2018).
9. M. Jermyn, K. Mok, J. Mercier, J. Desroches, J. Pichette, K. Saint-Arnaud, L. Bernstein, M. C. Guiot, K. Petrecca, and F. Leblond, "Intraoperative brain cancer detection with Raman spectroscopy in humans," Sci. Transl. Med. **7**(274), 274ra19 (2015).
10. D. Wirth, T. W. Smith, R. Moser, and A. N. Yaroslavsky, "Demeclocycline as a contrast agent for detecting brain neoplasms using confocal microscopy," Phys. Med. Biol. **60**(7), 3003–3011 (2015).
11. D. S. Kepshire, S. L. Gibbs-Strauss, J. A. O'Hara, M. Hutchins, N. Mincu, F. Leblond, M. Khayat, H. Dehghani, S. Srinivasan, and B. W. Pogue, "Imaging of glioma tumor with endogenous fluorescence tomography," J. Biomed. Opt. **14**(3), 030501 (2009).
12. M. C. Skala, K. M. Riching, D. K. Bird, A. Gendron-Fitzpatrick, J. Eickhoff, K. W. Eliceiri, P. J. Keely, and N. Ramanujam, "In vivo multiphoton fluorescence lifetime imaging of protein-bound and free nicotinamide adenine dinucleotide in normal and precancerous epithelia," J. Biomed. Opt. **12**(2), 024014 (2007).
13. Y. Sun, N. Hatami, M. Yee, J. Phipps, D. S. Elson, F. Gorin, R. J. Schrot, and L. Marcu, "Fluorescence lifetime imaging microscopy for brain tumor image-guided surgery," J. Biomed. Opt. **15**(5), 056022 (2010).
14. J. R. Lakowicz, *Principles of Fluorescence Spectroscopy* (Plenum Press, 1983).
15. J. P. Tardivo, A. Del Giglio, C. S. de Oliveira, D. S. Gabrielli, H. C. Junqueira, D. B. Tada, D. Severino, R. de Fátima Turchiello, and M. S. Baptista, "Methylene blue in photodynamic therapy: From basic mechanisms to clinical applications," Photodiagn. Photodyn. Ther. **2**(3), 175–191 (2005).
16. R. E. Kast, "Inhibiting the NLRP3 inflammasome with methylene blue as treatment adjunct in myelodysplasia," Front. Oncol. **8**(1), 280 (2018).
17. M. Snuderl, D. Wirth, S. A. Sheth, S. K. Bourne, C. S. Kwon, M. Ancukiewicz, W. T. Curry, M. P. Frosch, and A. N. Yaroslavsky, "Dye-enhanced multimodal confocal imaging as a novel approach to intraoperative diagnosis of brain tumors," Brain Pathol. **23**(1), 73–81 (2013).

Biomedical Optics EXPRESS

18. D. Wirth, M. Snuderl, S. Sheth, C. S. Kwon, M. P. Frosch, W. Curry, and A. N. Yaroslavsky, "Identifying brain neoplasms using dye-enhanced multimodal confocal imaging," J. Biomed. Opt. **17**(2), 026012 (2012).
19. A. N. Yaroslavsky, V. Neel, and R. R. Anderson, "Fluorescence polarization imaging for delineating nonmelanoma skin cancers," Opt. Lett. **29**(17), 2010–2012 (2004).
20. R. Patel, A. Khan, M. Kamionek, D. Kandil, R. Quinlan, and A. N. Yaroslavsky, "Delineating breast ductal carcinoma using combined dye-enhanced wide-field polarization imaging and optical coherence tomography," J. Biophotonics **6**(9), 679–686 (2013).
21. R. Patel, A. Khan, R. Quinlan, and A. N. Yaroslavsky, "Polarization-sensitive multimodal imaging for detecting breast cancer," Cancer Res. **74**(17), 4685–4693 (2014).
22. A. N. Yaroslavsky, X. Feng, Y. Ramirez, Y. Huang, A. Ross, and M. R. Hamblin, "Detecting brain cancer using fluorescence polarization imaging," Proc. SPIE, 1048017 (2018).
23. A. N. Yaroslavsky, X. Feng, A. Muzikansky, and M. R. Hamblin, "Fluorescence polarization of methylene blue as a quantitative marker of breast cancer at the cellular level," Sci. Rep. **9**(1), 940 (2019).
24. S. Malik, P. Jermain, X. Feng, and A. N. Yaroslavsky, "Multimodal optical imaging of renal cells," Opt. Eng. **58**(8), 082415 (2019).
25. J. Siegel, K. Suhling, S. Leveque-Fort, S. E. D. Webb, D. M. Davis, D. Phillips, Y. Sabharwal, and P. M. W. French, "Wide-field time-resolved fluorescence anisotropy imaging (TR-FAIM): imaging the rotational mobility of a fluorophore," Rev. Sci. Instrum. **74**(1), 182–192 (2003).
26. E. Kardash, J. Bandemer, and E. Raz, "Imaging protein activity in live embryos using fluorescence resonance energy transfer biosensors," Nat. Protoc. **6**(12), 1835–1846 (2011).
27. D. Gabrielli, E. Belisle, D. Severino, A. J. Kowaltowski, and M. S. Baptista, "Binding, aggregation and photochemical properties of methylene blue in mitochondrial suspensions," Photochem. Photobiol. **79**(3), 227–232 (2004).
28. F. Rashid and R. W. Horobin, "Interaction of molecular probes with living cells and tissues. Part 2. A structure-activity analysis of mitochondrial staining by cationic probes, and a discussion of the synergistic nature of image-based and biochemical approaches," Histochemistry **94**(3), 303–308 (1990).
29. D. J. Ball, Y. Luo, D. Kessel, J. Griffiths, S. B. Brown, and D. I. Vernon, "The induction of apoptosis by a positively charged methylene blue derivative," J. Photochem. Photobiol. B **42**(2), 159–163 (1998).
30. M. Wainwright, D. A. Phoenix, L. Rice, S. M. Burrow, and J. Waring, "Increased cytotoxicity and phototoxicity in the methylene blue series via chromophore methylation," J. Photochem. Photobiol. B **40**(3), 233–239 (1997).
31. R. Santus, C. Kohen, E. Kohen, J. P. Reyftmann, P. Morliere, L. Dubertret, and P. M. Tocci, "Permeation of lysosomal membranes in the course of photosensitization with methylene blue and hematoporphyrin: study by cellular microspectrofluorometry," Photochem. Photobiol. **38**(1), 71–77 (1983).
32. A. Rück, T. Köllner, A. Dietrich, W. Strauss, and H. Schneckenburger, "Fluorescence formation during photodynamic therapy in the nucleus of cells incubated with cationic and anionic water-soluble photosensitizers," J. Photochem. Photobiol. B **12**(4), 403–412 (1992).
33. D.-S. Yu, S.-Y. Chang, and C.-P. Ma, "The effect of methylene blue-sensitized photodynamic treatment on bladder cancer cells: a further study on flow cytometric basis," J. Urol. **149**(5), 1198–1201 (1993).
34. E. Demidenko, *Mixed Models: Theory and Applications with R* (Wiley, 2013).
35. G. Marconi and R. Quintana, "Methylene blue dyeing of cellular nuclei during salpingoscopy, a new in-vivo method to evaluate vitality of tubal epithelium," Hum. Reprod. **13**(12), 3414–3417 (1998).
36. T. F. Schmidt, L. Caseli, O. N. Oliveira, Jr., and R. Itri, "Binding of methylene blue onto Langmuir monolayers representing cell membranes may explain its efficiency as photosensitizer in photodynamic therapy," Langmuir **31**(14), 4205–4212 (2015).
37. L. Guntuku, V. G. Naidu, and V. G. Yerra, "Mitochondrial dysfunction in gliomas: pharmacotherapeutic potential of natural compounds," Curr. Neuropharmacol. **14**(6), 567–583 (2016).
38. L. B. Chen, "Mitochondrial membrane potential in living cells," Annu. Rev. Cell Biol. **4**(1), 155–181 (1988).
39. T. L. Chiu and C. C. Su, "Tanshinone IIA induces apoptosis in human lung cancer A549 cells through the induction of reactive oxygen species and decreasing the mitochondrial membrane potential," Int. J. Mol. Med. **25**(2), 231–236 (2010).
40. Z. Yang, Y. He, J.-H. Lee, N. Park, M. Suh, W.-S. Chae, J. Cao, X. Peng, H. Jung, C. Kang, and J. S. Kim, "A self-calibrating bipartite viscosity sensor for mitochondria," J. Am. Chem. Soc. **135**(24), 9181–9185 (2013).